OPTICA

Broadband depolarized perfect Littrow diffraction with multilayer freeform metagratings

Siyu Dong,[1,2,3,4,†] **Zhanyi Zhang,**[1,2,3,4,†] **Lingyun Xie,**[1,2,3,4,†] **Jingyuan Zhu,**[1,2,3,4]
Haigang Liang,[1,2,3,4] **Zeyong Wei,**[1,2,3,4] **Yuzhi Shi,**[1,2,3,4] **Alexander V. Tikhonravov,**[5]
Zhanshan Wang,[1,2,3,4,6,8] **Lei Zhou,**[7,*] **and Xinbin Cheng**[1,2,3,4,6,9]

[1]*Institute of Precision Optical Engineering, School of Physics Science and Engineering, Tongji University, Shanghai 200092, China*
[2]*MOE Key Laboratory of Advanced Micro-Structured Materials, Shanghai 200092, China*
[3]*Shanghai Frontiers Science Center of Digital Optics, Shanghai 200092, China*
[4]*Shanghai Professional Technical Service Platform for Full-Spectrum and High-Performance Optical Thin Film Devices and Applications, Shanghai 200092, China*
[5]*Research Computing Center, Moscow State University, Leninskie Gory, Moscow 199992, Russia*
[6]*Shanghai Institute of Intelligent Science and Technology, Tongji University, Shanghai 200092, China*
[7]*State Key Laboratory of Surface Physics, Key Laboratory of Micro and Nano Photonic Structures (Ministry of Education) and Department of Physics, Fudan University, Shanghai 200438, China*
[8]*wangzs@tongji.edu.cn*
[9]*chengxb@tongji.edu.cn*
[†]*These authors contributed equally to this paper.*
phzhou@fudan.edu.cn

Littrow diffraction, the ability to reflect light back along incident direction, is a key functionality of retroreflectors, exhibiting wide applications in nanophotonics. However, retroreflectors have hitherto low working efficiencies and narrow bandwidths, and work only for a specific polarization, being unfavorable for integration-optics applications. Here, we propose a type of metagrating consisting of an all-dielectric Bragg reflector and a periodic metasurface with freeform-shaped dielectric resonators, which enables broadband depolarized perfect Littrow diffraction at optical frequencies. The physics is governed by exact cancellations of specular reflections contributed by two Bragg modes in metagratings, enabled by careful structural optimization to yield the desired reflection-phase difference of Bragg modes within a wide frequency band and for two polarizations. As a proof of concept, we experimentally demonstrate retroreflections with unpolarized absolute efficiency higher than 98% (99% in design) at 1030–1090 nm using multilayer freeform metagratings. Our results pave the way for numerous applications based on high-efficiency Littrow diffraction (e.g., spectral laser beam combining), which is not bonded to a specific polarization or frequency. © 2023 Optica Publishing Group under the terms of the Optica Open Access Publishing Agreement

https://doi.org/10.1364/OPTICA.486332

1. INTRODUCTION

The widest and probably simplest way to back direct the flow of electromagnetic waves along its incident direction in photonics is impinging it on diffraction gratings at the so-called Littrow angle [1]. Gratings used for retroreflection purposes are known as blazed gratings, for example, metal echelette gratings [2] or multilayer dielectric gratings [3–5]. Yet, developing Littrow diffraction in a broadband domain with extremely high efficiencies and no polarization independence remains tremendously challenging. Potential applications for this significant aim include compact spectrometers [6], information and communication technology [7], pulse compression [8], spectral combining [9], and so forth [10,11]. Technically, the desired broadband depolarized perfect Littrow diffraction is a long-standing bottleneck for the most traditional diffraction gratings. Specifically, their sawtooth edges for metal echelette gratings typically lead to undesired efficiency limitations, while dielectric gratings are usually featured with strong polarized dependence because they are naturally anisotropic in geometry.

Recent decades have witnessed the emergence of metamaterials/metasurfaces [12–26] that provide unprecedented capabilities to engineer electromagnetic waves in an arbitrary manner. For example, the widely studied phase-gradient metasurfaces [27–33] have been demonstrated to flexibly manipulate the wavefront, amplitude, and polarization of light. However, such gradient metasurfaces typically operate well in a regime of proper Littrow angles while suffering from low efficiencies for large bending angles [34], especially at optical frequencies, because they require to discretize a continuous, fast-varying impedance profile per period. A different route proposed by Alu and co-workers suggests that a perfect wavefront transformation at a large Littrow angle can also be achieved using periodic arrays of one or two suitably tailored

inclusions, called metagratings [35]. However, the functionality of broadband depolarized perfect Littrow diffraction has not yet been reported with metagratings. For instance, although a Littrow-like perfect anomalous reflection has been demonstrated using metallic metagratings in the microwave region [36], their results are polarization dependent, and efficiencies in the broadband domain unfortunately drop; metallic structures are also highly lossy at optical frequencies. Moreover, although many dielectric metagratings [37–40] including the emergent freeform metagratings [41–43] have been investigated, they all typically suffer from transmission losses and do not necessarily exhibit the desired depolarized and broadband performances. Therefore, realizing broadband depolarized perfect Littrow diffraction still remains a great challenge for the nanophotonics community.

In this work, we propose a novel idea of multilayer freeform metagratings, consisting of a dielectric multilayer Bragg reflector and a periodic metasurface composed of dielectric resonators with a freeform shape, to enable the desired broadband depolarized perfect Littrow diffraction. These all-dielectric structures are not only immune to absorption losses but also improve the amplitude control by using multilayer high-reflection films to eliminate all transmission losses. Moreover, the scatterings of Bragg modes that determine the final broadband efficiencies can be fully controlled by customizing both phase difference $\Delta\Phi$ and phase-difference dispersion $\partial\Delta\Phi/\partial\omega$ of two Bragg modes when fine-tuning their propagation phase and interfacial phase. Therefore, optimizing the geometric shape of metasurfaces can provide adequate degrees of freedom to help achieve the desired $\Delta\Phi$ and $\partial\Delta\Phi/\partial\omega$ required by broadband depolarized perfect Littrow diffraction. As a proof of concept, we deploy this technique to demonstrate a typical potential application, i.e., spectral laser beam combining, which exhibits an unpolarized absolute efficiency higher than 99% at 1030–1090 nm at a Littrow angle of 36° (corresponding 72° bending angle). The experimental result shows unpolarized broadband efficiencies over 98%.

2. MODEL OF BROADBAND DEPOLARIZED PERFECT LITTROW DIFFRACTION

Figure 1(a) illustrates the reflection from a mirror, Littrow diffraction, and broadband Littrow diffraction for the gratings. The mirror reflection does not change the horizontal component of the momentum of incident light ($\boldsymbol{p}_x^i$), while Littrow diffraction flips the direction of $\boldsymbol{p}_x^i$ by adding a particular grating momentum, that is, $\boldsymbol{p}_g = -2\boldsymbol{p}_x^i$. Broadband Littrow diffraction in spectral beam combining is an inverse process of spectral dispersion, where an identical horizontal momentum component ($\boldsymbol{p}_g$) is added to each $\boldsymbol{p}_x^i$ to get the same outgoing direction. Figure 1(b) shows the k-space operation of the gratings with a period Λ_g and reciprocal lattice vector $k_g = 2\pi/\Lambda_g$, where the location of arrows in reflection depicts multiple Floquet modes with different k_x^r. Here, we can design the system to allow only two reflection channels (i.e., the zeroth and −1st order channels fall within the propagation range of $k_x^r \in [-k_0, k_0]$) by aligning the proper k_x^i and k_g, while all other high-order channels are evanescent.

To maximize the efficiency of the −1st order reflection, a coupled-resonator model based on the mode-expansion theory [44] is adopted to give insight into the high-efficiency diffraction process in this structural system. As shown in Fig. 2(a), the incident plane wave first couples into the dielectric waveguide structures in the form of a set of Bragg modes. Then, these modes can propagate, reflect, and finally couple out into the external-field channels. In this way, every mode distributes its energy to all possible far-field diffraction orders. Supposing that the structural depth is large enough so that the evanescent modes do not participate in the energy transfer, the highest efficiency in the −1st order reflection is achieved when all out-coupled propagating modes in the zeroth order channel could strongly destructively interfere because of energy conservation, since the bottom multilayer reflection mirror will make all the energy eventually couple into the reflection orders.

In general, a clean system is usually desirable so that we can design the system to support only two propagating Bragg modes
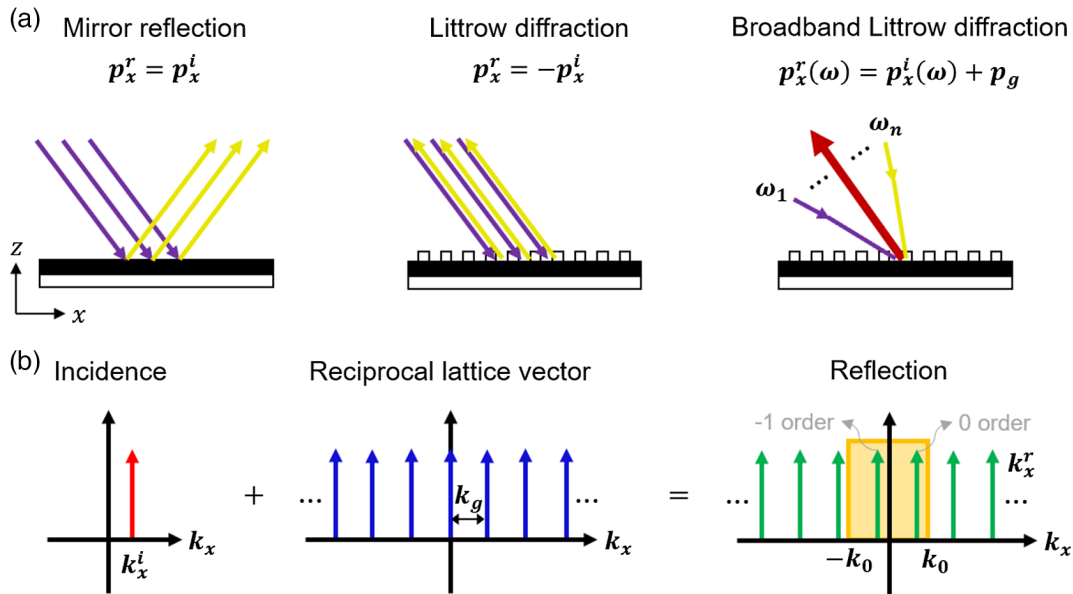

Fig. 1. Littrow diffraction concept. (a) Schematic illustration of reflection by a mirror, Littrow diffraction, and broadband Littrow diffraction. The mirror does not change the horizontal component of the momentum ($\boldsymbol{p}_x^i$) of the incidence, while Littrow gratings add a momentum ($\boldsymbol{p}_g$) to it and change its direction. (b) Diagram describing how Littrow gratings operate in k-space. Arrows indicate the existence of diffraction modes, and their locations depict the magnitude of k_x^r; the orange box denotes the regime of propagation waves.
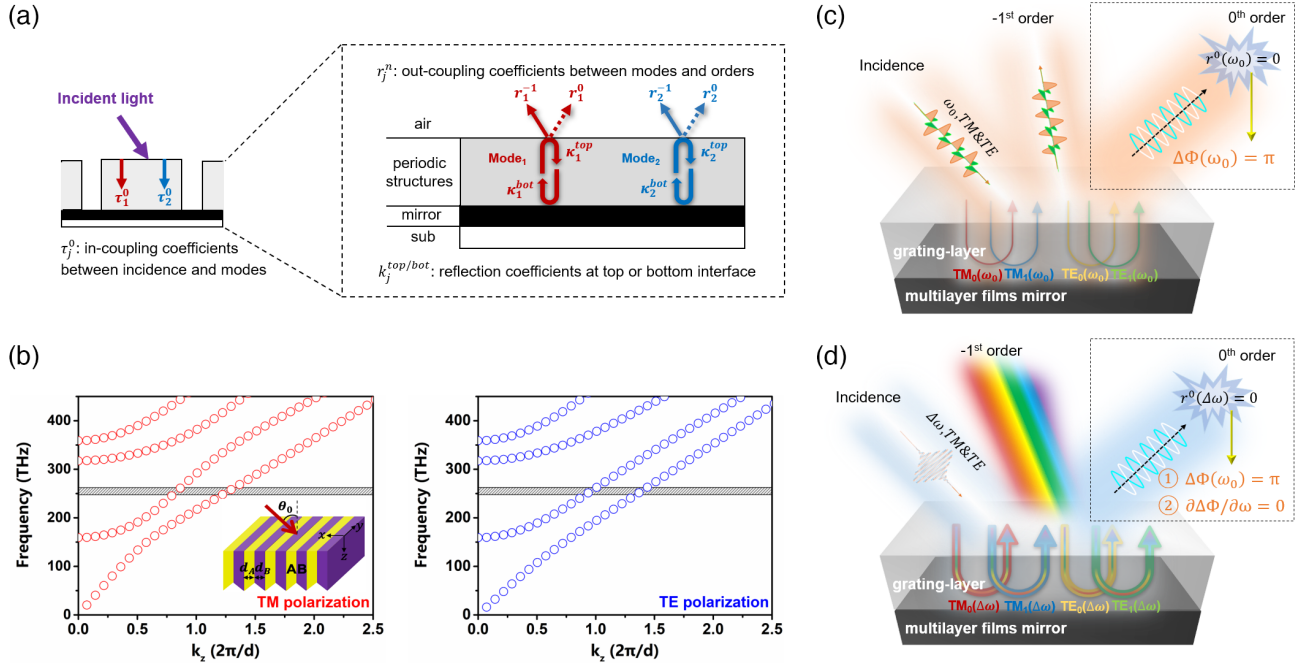
Fig. 2. Theoretical model of depolarized broadband perfect Littrow diffraction. (a) When incident light interacted with the structures, the energy first coupled into Bragg modes in the structures with the in-coupling coefficient τ_j^0. Then, the propagating modes propagated inside the structural layer and were reflected at the interfaces with the reflection coefficient $k_j^{\text{top}}/k_j^{\text{bot}}$; finally, they coupled out into the reflection diffraction channels with the out-coupling coefficient r_j^n. (b) Band structures of k_z and ω of 1D gratings with duty ratio of 0.5 calculated by TMM [Eq. (1) and (2)], illustrating that only two modal dispersion curves can be intersected in our concerned frequency range (shadow region) for both TM and TE states when setting the period $\Lambda_g = 905$ nm and incident angle $\theta_0 = 36°$. The inset depicts the schematic picture under study, where $\varepsilon_A = 4, \varepsilon_B = 1, \mu_A = \mu_B = 1$. (c) Physical picture of single-wavelength depolarized high-efficiency diffraction. Perfect efficiency in -1st order reflection occurs when the out-coupled modes in zeroth order reflection strongly destructively interfere. (d) Physical picture of broadband depolarized high-efficiency diffraction. The broadband destructive interference in zeroth order reflection should be satisfied for both TM and TE states.

by altering the period and the incident angle. We can assume that the grating layer is an infinite-length dielectric waveguide slab to study the corresponding band structures. Taking one-dimensional (1D) gratings as the example, a straightforward calculation using the transfer matrix method (TMM) shows that, given a frequency ω and $k_0 = \omega/c$, the vertical wave vector k_z of eigenmodes is correlated with the horizontal wave vector k_x by the following equations [45]:

$$2\cos(k_x^A d_A + k_x^B d_B) - \left(\frac{\sigma_B k_x^A}{\sigma_A k_x^B} + \frac{\sigma_A k_x^B}{\sigma_B k_x^A} - 2\right)$$

$$\times \sin(k_x^A d_A)\sin(k_x^B d_B) = 2\cos(k_x d), \quad (1)$$

and

$$k_x^A = \sqrt{\varepsilon_A \mu_A k_0^2 - (k_z)^2}, \quad k_x^B = \sqrt{\varepsilon_B \mu_B k_0^2 - (k_z)^2}, \quad (2)$$

where $\sigma_j = \mu_j$ for TE polarization and $\sigma_j = \varepsilon_j$ for TM polarization, and each unit cell Λ_g contains two layers with thicknesses d_A, d_B and electromagnetic parameters $\varepsilon_A, \mu_A, \varepsilon_B, \mu_B$. By fixing $k_x = k_0 \cdot \sin(\theta_0)$, solving Eq. (1) yields a series of real k_z for all eigenmodes, and then, the corresponding dispersion curves of the band structures of k_z can be easily obtained, as shown in Fig. 2(b) (the inset depicts the schematic picture under study here). With a well-defined period and incident angle, here, $\Lambda_g = 905$ nm and $\theta_0 = 36°$, it can be seen that there are always two propagating modes (fundamental mode and first high-order mode) involved

in the considered frequency range for both TM and TE states, for example, 1030–1090 nm (275.2–291.3 THz).

The underlying principle of depolarized high efficiency is first explored for single-wavelength Littrow diffraction, that is, the phase difference $\Delta\Phi$ of two out-coupled Bragg modes in the zeroth order should be π to satisfy the canceling condition for each polarization state [see Fig. 2(c)]. Then, broadband requirements are further explored, wherein, besides the single-wavelength demand of $\Delta\Phi = \pi$, the phase-difference dispersion $\partial\Delta\Phi/\partial\omega$ should be considered in approaching zero, aiming at a constant cancellation in the broadband domain [see Fig. 2(d)]. Next, how to satisfy the desired $\Delta\Phi$ and $\partial\Delta\Phi/\partial\omega$ demands with what kind of particular structures is explained. Finally, the multilayer freeform metagratings with unpolarized broadband efficiencies higher than 99% at 1030–1090 nm can be achieved.

A. Phase-Difference Requirement for Depolarized High Efficiency at Single Wavelength

First, the single-wavelength and single-polarization case was analyzed. The reflection coefficient of the zeroth order r^0 can be written as

$$r^0 = U_1^0 + U_2^0, \quad (3)$$

where U_j^0 denotes the complex amplitude of the jth out-coupling mode in the zeroth order reflection. The highest efficiency in the -1st order is achieved when $r^0 = 0$, as shown in Fig. 2(c). Therefore, U_1^0 and U_2^0 should satisfy the specific phase difference

and amplitude criteria to cancel each other out. Since their amplitudes $|U_1^0|$ and $|U_2^0|$ are almost equal when illuminated around the Littrow mounting (see Fig. S2 in Supplement 1 Note 1), the core demand is that their phase difference $\Delta\Phi$ should satisfy

$$\Delta\Phi = \arg(U_1^0) - \arg(U_2^0) = \pi. \tag{4}$$

For the actually finitely thick dielectric waveguide nanopillar structures, the concerned modal phase $\arg(U_j^0)$ is composed of two contributions: propagation phase Φ_t and interfacial phase Φ_c. Considering the low Q-factor resonance of Bragg modes (detailed demonstrations are given in Supplement 1 Note 4), it is reasonable to think that the first bounding process of Bragg modes inside the structural layer is dominant while ignoring the multiple scattering. At this moment, Φ_t and Φ_c can be written as

$$\Phi_t = 2k_0 n_{\text{eff}} h, \tag{5}$$

which is determined by the modal effective index n_{eff} and thickness of grating-layer h, and

$$\Phi_c = \arg(\tau_j^0) + \arg(r_j^0) + \arg(\kappa_j^{\text{bot}}), \tag{6}$$

where $\arg(\tau_j^0)$ and $\arg(r_j^0)$ are in-coupling phase and out-coupling phase at the top air–grating interface, respectively, and $\arg(\kappa_j^{\text{bot}})$ is the reflection phase at the bottom grating–mirror interface (detailed derivations are given in Supplement 1 Note 1).

In this way, the phase difference $\Delta\Phi$ can be further written as

$$\Delta\Phi = \Delta\Phi_t + \Delta\Phi_c = (2k_0\Delta n_{\text{eff}} h) + (\Phi_{c1} - \Phi_{c2})$$

$$= \Delta\Phi_t + o(\Delta\Phi), \tag{7}$$

with $\Delta n_{\text{eff}} = n_{\text{eff}1} - n_{\text{eff}2}$. It should be mentioned that the propagation phase difference $\Delta\Phi_t$ actually plays a dominant role in adjusting $\Delta\Phi$ here, because $\Delta\Phi_t$ has an overwhelming quantity compared to $\Delta\Phi_c$ in such thick waveguide structures (see Fig. S3d in Supplement 1 Note 2). Therefore, it is usually easy to achieve high efficiency at a single wavelength and single polarization by using numerous combinations of Δn_{eff} and h to build a $\Delta\Phi$ of π.

Moreover, to further eliminate the polarization dependence, it is necessary to have $\Delta\Phi_{\text{TM}} = \Delta\Phi_{\text{TE}} = \pi$ by considering two pairs of Bragg modes (TM and TE) simultaneously. In this way, a depolarized Δn_{eff} is the key condition for depolarized high efficiency at a single wavelength as

$$\Delta n_{\text{eff(TM)}} = \Delta n_{\text{eff(TE)}}, \tag{8}$$

because the propagation phase is key in this issue. Once Δn_{eff} has been determined, we should adjust the thickness h to make sure $\Delta\Phi_t$ is close to π. Therefore, Δn_{eff} must also be of adequate size; otherwise, the thickness h would be too large to realize in practice.

B. Phase Difference and Phase-Difference Dispersion Requirements for Depolarized Broadband High Efficiency

To further consider broadband diffraction, the broadband phase difference $\Delta\Phi(\omega)$ should be roughly constant of π in the appointed bandwidth to reach the broadband destructive interference, as shown in Fig. 2(d). In this way, besides the satisfaction of the single-point phase-difference requirement $\Delta\Phi_{\text{TM}}(\omega_0) = \Delta\Phi_{\text{TE}}(\omega_0) = \pi$, how to achieve the desired phase-difference broadband dispersion nature, for example,

$$\frac{\partial\Delta\Phi_{\text{TM}}}{\partial\omega} = \frac{\partial\Delta\Phi_{\text{TE}}}{\partial\omega} = 0, \tag{9}$$

is the additional challenge in the broadband issue. Here, we can assume that $\Delta\Phi$ is almost linearly dispersive in our concerned bandwidth, and thus $\partial\Delta\Phi/\partial\omega_0$ can be represented as the gradient in the whole bandwidth.

Similarly, the derivative of phase difference $\partial\Delta\Phi/\partial\omega_0$ can also be divided into two contributions from both the propagation phase difference and interfacial phase difference, which can be written as

$$\frac{\partial\Delta\Phi}{\partial\omega_0} = \frac{\partial\Delta\Phi_t}{\partial\omega_0} + \frac{\partial\Delta\Phi_c}{\partial\omega_0} = \frac{\partial(k_0\Delta n_{\text{eff}}2h)}{\partial\omega_0} + \frac{\partial\Delta\Phi_c}{\partial\omega_0}$$

$$= \frac{\partial\Delta\Phi_c}{\partial\omega_0} + o\left(\frac{\partial\Delta\Phi}{\partial\omega_0}\right). \tag{10}$$

It is worth noting that the derivative of propagation-phase difference $\partial\Delta\Phi_t/\partial\omega_0 \approx 2k_0\Delta n_{\text{eff}}h/\omega_0 = \pi/\omega_0$ is intrinsically small, and for a finite spectral bandwidth, the total dispersion variation of $\Delta\Phi_t$ is thus expected to be very small. In this way, the derivative of interfacial phase difference $\partial\Delta\Phi_c/\partial\omega_0$—of course, the dispersion variation of $\Delta\Phi_c$—plays a dominant role in the final broadband performance (see Fig. S3d in Supplement 1 Note 2). Thus, a depolarized $\partial\Delta\Phi_c/\partial\omega_0$ with the quantity as small as possible is the key condition for depolarized broadband high efficiency.

C. Effect of Structural Geometry on Phase Difference and Phase-Difference Dispersion

Now, the question is: what kind of structures can exhibit such a desired phase difference and phase-difference dispersion tailoring ability? We note that, on one hand, the Bragg modes are eigenmodes, whose Δn_{eff} are dependent only on the waveguide cross section, that is, the lateral structural design (e.g., duty ratio), which is characterized by the vertical wave vector k_z described as

$$\Delta n_{\text{eff}} = \frac{\Delta k_z}{k_0}. \tag{11}$$

On the other hand, the derivative of the interfacial phase difference $\partial\Delta\Phi_c/\partial\omega_0$ is also highly related to lateral structures, which transforms the lateral field distributions of eigenmodes to impact the coupling coefficients between the external waves and internal excited modes to affect the interfacial phase and interfacial phase dispersion [46]. Therefore, the lateral structures are predominant degrees of freedom in tailoring both Δn_{eff} and $\partial\Delta\Phi_c/\partial\omega_0$ (detailed demonstrations are given in Supplement 1 Note 2).

Here, typical materials HfO_2 and SiO_2 and a typical architecture comprising a grating layer, spacer film, and multilayer high-reflection mirror were used to design broadband depolarized perfect Littrow diffraction [47]. Three kinds of structures, including multilayer 1D gratings, multilayer 2D rectangular nanopillars, and multilayer 2D compound rectangular nanopillars, which possess the incremental level of the lateral degrees of freedom, are compared with their tailoring ability on $\Delta n_{\text{eff(TM)}}$, $\Delta n_{\text{eff(TE)}}$, $\partial\Delta\Phi_{c(\text{TM})}/\partial\omega$, and $\partial\Delta\Phi_{c(\text{TE})}/\partial\omega$, as shown in Fig. 3.

For the multilayer 1D gratings in Fig. 3(a), due to only one lateral degree of freedom (e.g., grating duty ratio), the combinations of $\Delta n_{\text{eff(TM)}}$ and $\Delta n_{\text{eff(TE)}}$ at central frequency ω_0 have only a limited coverage (red dots) because they are associated when tuning the duty ratio f, as shown in Fig. 3(b). Note that a single

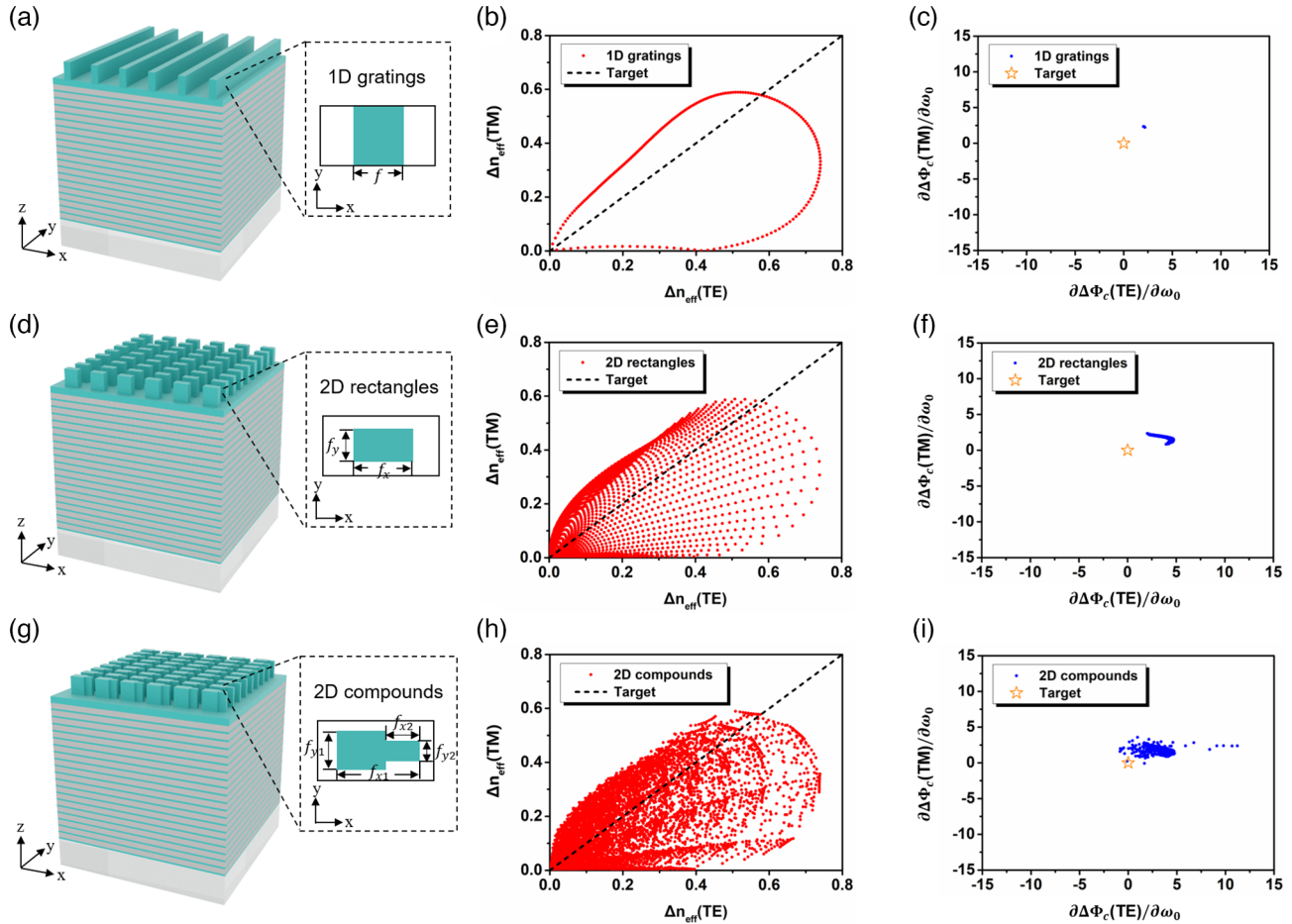**Fig. 3.** Comparison of three kinds of structures with different lateral degrees of freedom to their control ability on Δn_{eff} and $\partial \Delta \Phi_c / \partial \omega_0$. (a) Schematic of multilayer 1D gratings with only one lateral degree of freedom. (b) $\Delta n_{eff(TM)}$ and $\Delta n_{eff(TE)}$ combinations realized by 1D gratings are shown using red dots. The dotted line represents the target of depolarized Δn_{eff}. (c) The corresponding $\partial \Delta \Phi_{c(TM)} / \partial \omega_0$ and $\partial \Delta \Phi_{c(TE)} / \partial \omega_0$ combinations of the depolarized points in (b) with $\Delta n_{eff} > 0.3$ are given using blue dots, which are far away from the ideal target of $\partial \Delta \Phi_c / \partial \omega_0$, marked by an orange pentagram. (d) Schematic of multilayer 2D rectangular nanopillars with two lateral degrees of freedom and (e) their $\Delta n_{eff(TM)}$ and $\Delta n_{eff(TE)}$ combinations, which exhibit extensive coverage compared to 1D gratings. (f) Their corresponding $\partial \Delta \Phi_{c(TM)} / \partial \omega_0$ and $\partial \Delta \Phi_{c(TE)} / \partial \omega_0$ combinations are still distinct from the ideal target due to inadequate degrees of freedom. (g) Schematic of multilayer 2D compound rectangular nanopillars with four degrees of freedom and (h) their $\Delta n_{eff(TM)}$ and $\Delta n_{eff(TE)}$ combinations, which exhibit the same coverage but enriched database compared to 2D rectangular nanopillars. (i) Their corresponding $\partial \Delta \Phi_{c(TM)} / \partial \omega_0$ and $\partial \Delta \Phi_{c(TE)} / \partial \omega_0$ combinations can well cover the ideal target due to adequate lateral degrees of freedom. The structures in (a), (d), and (g) consist of the top HfO_2 structural layer, HfO_2 spacer layer, and bottom HfO_2/SiO_2 multilayer reflection films with the stack of (H2L)[20]. The refractive indices of high- and low-index layers are $n_H = 2.0$ and $n_L = 1.45$, and their thicknesses are $d_H = 94$ nm and $d_L = 267$ nm, respectively. $\partial \Delta \Phi_c / \partial \omega_0$ in (c), (f), and (i) was calculated when the thickness of the spacer was arbitrarily set to 160 nm (other values are also feasible), and the height of the gratings are fixed with Δn_{eff} to make sure the propagation phase difference $\Delta \Phi_t (\omega_0) = \pi$.

intersection with the target dotted line means that only a specific duty ratio (that is, $f = 0.45$; see Fig. S3c in Supplement 1 Note 2) can exactly provide a desired depolarized Δn_{eff}. At this point, 1D gratings can build a depolarized propagation phase difference $\Delta \Phi_t$ to achieve single-wavelength unpolarized high efficiency. However, when further examining the corresponding $\partial \Delta \Phi_c / \partial \omega_0$, we can see that this duty ratio fails to realize the desired $\partial \Delta \Phi_{c(TM)} / \partial \omega_0$ and $\partial \Delta \Phi_{c(TE)} / \partial \omega_0$ combination simultaneously, as shown in Fig. 3(c), because the lateral degree of freedom has been completely fixed by the depolarization of Δn_{eff}.

For the multilayer 2D rectangular nanopillars in Fig. 3(d), the Δn_{eff} combinations can cover anywhere within the framed scope because the duty ratio in both x and y directions can be arbitrarily tuned, as shown in Fig. 3(e). Since $\Delta n_{eff(TM)}$ and $\Delta n_{eff(TE)}$ can almost be independently controlled, a set of depolarized Δn_{eff} combinations is easily obtained. We can filter out the duty ratios

with depolarized and adequate-sized Δn_{eff} (e.g., $\Delta n_{eff} > 0.3$), and then examine their corresponding $\partial \Delta \Phi_c / \partial \omega_0$. Unfortunately, as shown in Fig. 3(f), they still fail to realize the target of $\partial \Delta \Phi_c / \partial \omega_0$ combination by using 2D rectangular nanopillars. This is because duty ratios f_x and f_y are still to some extent fixed by the depolarization of Δn_{eff}, and lateral degrees of freedom are not enough yet to further customize $\partial \Delta \Phi_c / \partial \omega_0$. It reminds us that there should be more lateral degrees of freedom to fully control Δn_{eff} and $\partial \Delta \Phi_c / \partial \omega_0$ at different polarization states, as both depend on the lateral structures but in different mechanisms.

According to the principle of equivalence of degrees of freedom, it is expected that at least four effective lateral degrees of freedom can fully control the associated $\Delta n_{eff(TM)}$, $\Delta n_{eff(TE)}$, $\partial \Delta \Phi_{c(TM)} / \partial \omega_0$, and $\partial \Delta \Phi_{c(TE)} / \partial \omega_0$ for broadband depolarized perfect Littrow diffraction. Therefore, we next explore the multilayer 2D compound rectangular nanopillars in Fig. 3(g) with four

alterable duty ratios. It can be seen in Fig. 3(h) that, although the coverage scope of Δn_{eff} does not change, the database of the points with depolarized Δn_{eff} is greatly enriched, which can provide more possibilities to find an appropriate solution in $\partial\Delta\Phi_c/\partial\omega_0$ control. As shown in Fig. 3(i), the corresponding $\partial\Delta\Phi_c/\partial\omega_0$ combinations can successfully cover the target at this moment. We can understand this result from the perspective that there are enough degrees of freedom for 2D compound structures to impact the band structures of k_z to control $\Delta n_{eff(TM)}$ and $\Delta n_{eff(TE)}$, and modify the modal field profiles to adjust $\partial\Delta\Phi_{c(TM)}/\partial\omega_0$ and $\partial\Delta\Phi_{c(TE)}/\partial\omega_0$.

3. RESULTS

We have demonstrated that the depolarization and broad band for high-efficiency Littrow diffraction depend strongly on the lateral degrees of freedom of the top-layer structures. The advantage of the regular structures such as 1D gratings or rectangular nanopillars is their simplicity, but they also sacrifice versatility and capability in controlling Δn_{eff} and $\partial\Delta\Phi_c/\partial\omega$, resulting in a limited depolarized broadband performance. Here, to maximize the structural lateral degrees of freedom to enhance the depolarization and broadband dispersion control capability, we propose all-dielectric multilayer freeform metagratings that consist of a multilayer Bragg reflector and periodic freeform metagratings designed by adjoint-based topology optimization, which can allow the lateral structures to be freely varied to search for highly nonintuitive patterns with arbitrary geometric shapes. Here, a typical application for broadband depolarized perfect Littrow diffraction in spectral laser beam combining in the near-infrared is considered in our design. The concerned spectral range is 1030–1090 nm, which covers the main high-output wavelengths of fiber lasers. The combining beam is fixed at the −1st reflective Littrow mounting of central wavelength $\lambda_0 = 1064$ nm, where the Littrow angle θ_0 is set to 36° and the period $\Lambda_g = \lambda_0/2\sin\theta_0 = 905$ nm to build a dual-mode live system. The materials and coating stack of the multilayer mirror are the same as those used in Fig. 3.

In the optimization, we used the optimal design of 2D compound rectangular nanopillars in Fig. 3(i) achieved by scanning Δn_{eff} and $\partial\Delta\Phi_c/\partial\omega$ as the initial solution to optimize the shape
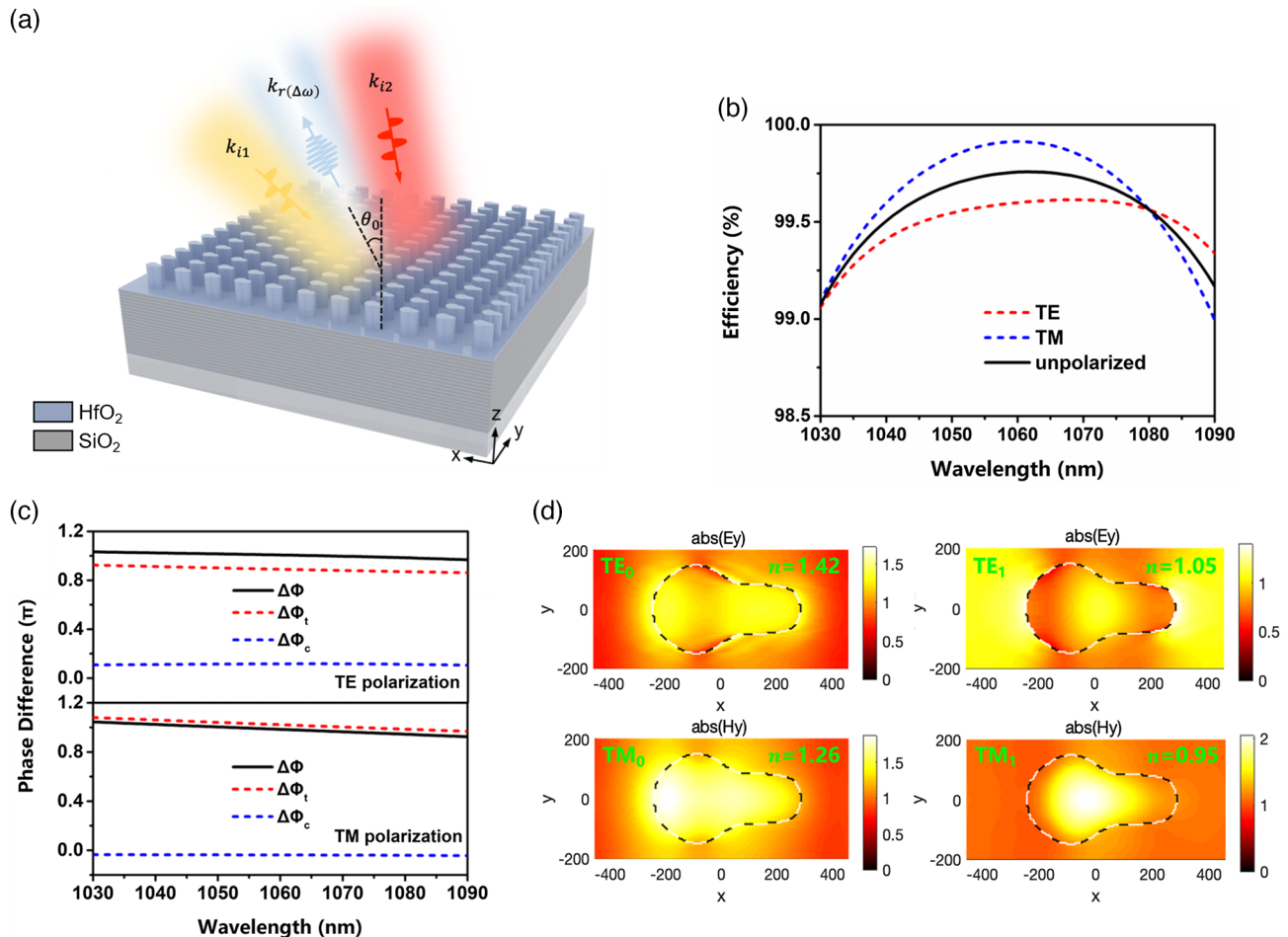

Fig. 4. Simulation of broadband depolarized perfect Littrow diffraction using multilayer freeform metagratings. (a) Schematic drawing of topology-optimized multilayer freeform metagratings. The top pattern layer is 2D periodic HfO₂ metagratings with a bulb-like shape designed by the topology optimization algorithm, aiming at a small broadband dispersion of $\Delta\Phi$ for both polarization states. The optimized height of metagratings and spacer thickness are 744 and 128 nm, respectively. (b) Theoretical broadband efficiency curves of multilayer freeform metagratings with higher than 99% unpolarized efficiency in the whole spectral range. (c) Broadband dispersion curves of $\Delta\Phi$ as well as the propagation phase difference $\Delta\Phi_t$ and interfacial phase difference $\Delta\Phi_c$ of the multilayer freeform metagratings. An almost constant broadband $\Delta\Phi$ of π at both polarization states brings remarkable highly unpolarized broadband efficiencies for multilayer freeform metagratings. (d) Mode field profiles of multilayer freeform gratings at central wavelength 1064 nm. An asymmetric profile is obviously distinct from the 1D gratings. The value labeled in the graph is the modal effective index. The dashed line represents the lateral contour of the metagratings.

and height of the metagratings as well as spacer thickness. The detailed optimization process is given in Section 6. The schematic of optimized multilayer freeform metagratings is shown in Fig. 4(a). It can be seen that the optimized result can be interpreted as the associated variant of the initial compound rectangular nanopillars. The performance realized by multilayer freeform metagratings is as follows. It can be seen in Fig. 4(b) that the broadband efficiencies are higher than 99% for both polarization states in the whole aimed spectral scope (results outside the spectral domain of interest are given in Fig. S6 in Supplement 1 Note 3). We can verify the broadband dispersion of the phase difference $\Delta\Phi$ as well as propagation phase difference $\Delta\Phi_t$ and interfacial phase difference $\Delta\Phi_c$ at different polarizations. In Fig. 4(c), we can see that the multilayer freeform metagratings can present an almost constant dispersion variation around π of $\Delta\Phi$ for both polarization states simultaneously because the dispersion variations of interfacial phase differences $\Delta\Phi_{c(TM)}$ and $\Delta\Phi_{c(TE)}$ are very small. The fundamental reason is attributed to the modification of the modal field of Bragg modes, whose field profiles are given in Fig. 4(d). Compared with the modal fields of 1D gratings (see Fig. S5d in Supplement 1 Note 2), we assume that it may be related to the asymmetry of the field since the incident fields and diffraction fields are also asymmetric, which can increase the field matching between them. In addition, the differences of field profiles between TE and TM modes of the freeform metagratings are much greater than those of 1D gratings, which we attribute to the better depolarizing ability of freeform metagratings.

In the experiments, multilayer freeform metagratings were fabricated by electron beam evaporation with ion-beam assisted deposition, electron beam lithography (EBL), atomic layer deposition (ALD), and inductively coupled reactive ion etching techniques. Taking advantage of the large-scale fabrication capability of the current EBL facility, we prepared a large-area sample of 10×10 mm^2 (or 5×5 mm^2), which can further implement mass copy by reproduction technology such as nanoimprint lithography. The detailed preparation process is given in Section 6. Figures 5(a)–5(d) give the scanning electron microscopy (SEM) images of fabricated multilayer freeform metagratings, showing relatively well-matched structural parameters with the design. For a better comparison, the designed pattern is plotted as the red pattern in Fig. 5(a), being almost consistent with our experimental result. The broadband efficiency spectrum of the sample was tested by an angle-resolved macroscopic spectrum system. The detailed spectral tests are discussed in Section 6 and Supplement 1 Note 7. As shown in Fig. 5(e), when we use the unpolarized source to perform the measurement, the results exhibit over 98% absolute efficiency in -1st order reflection from 1030–1090 nm (measurement results outside the spectral domain of interest are given in Fig. S6 in Supplement 1 Note 3). Admittedly, it is expected that the results have a random error estimated at about 1% because of the stability of the light source and mechanical vibration, but the current results are enough to show the validity of our work.

4. DISCUSSION

We realize broadband depolarized perfect Littrow diffraction by controlling the phase difference $\Delta\Phi$ and phase-difference dispersion $\partial\Delta\Phi/\partial\omega$ of Bragg modes in a metasystem, which comes from full control of their propagation phase $\Delta\Phi_t$ and interfacial phase dispersion $\partial\Delta\Phi_c/\partial\omega_0$ by adequate lateral degrees of freedom in
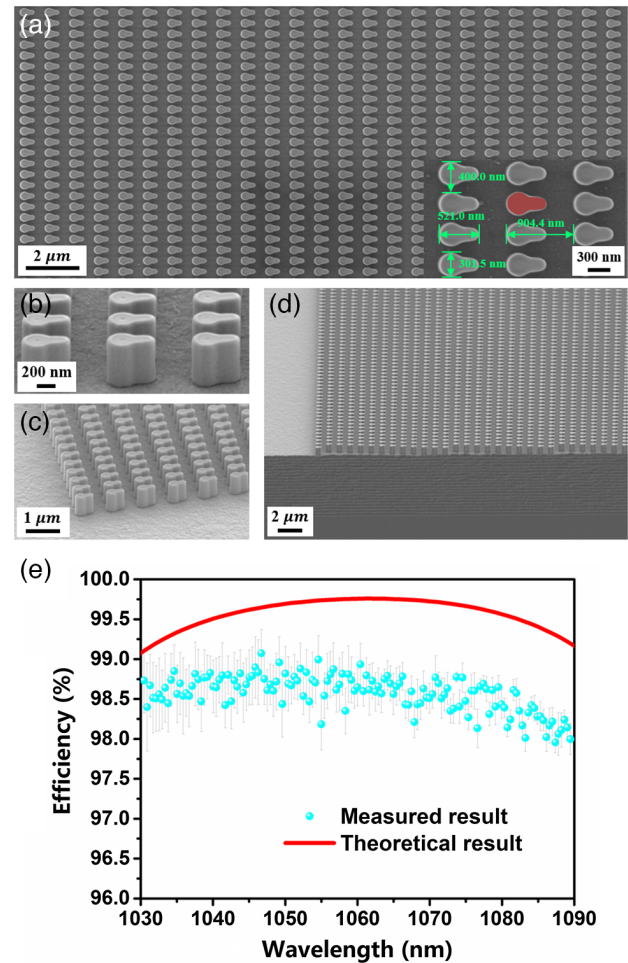

Fig. 5. Experimental results of multilayer freeform metagratings. (a)–(d) SEM images of the prepared sample. The red pattern in (a) denotes the design for comparison with the experimental result. (e) Diffraction efficiency spectra of the -1st order reflection. The red solid line is the theoretical design curve, and the blue dots are the experimentally measured results. The error bars donate the 95% confidence interval for five measurements given in Fig. S10d in Supplement 1.

our proposed multilayer freeform metagratings. This elegant strategy is straightforward and effective, because the freeform shape of metagratings can result in more flexible polarization responses and field distributions of Bragg modes, and multilayer films can help control the amplitude without loss. For example, in Supplement 1 Note 2, we present a comparison of our results with the performance realized by traditional multilayer 1D gratings to demonstrate the validity of our proposed methodology. In an additional example given in Supplement 1 Note 5, broadband depolarized perfect Littrow diffraction is also demonstrated using low-index material such as SiO$_2$ freeform metagratings, even though the material index is greatly reduced, which typically corresponds to a seriously diminished field tailoring capability as expected. Although the achieved bandwidth (about 40 nm) by SiO$_2$ metagratings is slightly less than that of HfO$_2$ metagratings, we believe that our powerful multilayer freeform metagratings can provide flexible degrees of freedom to advance the performance in diffractive optics. Moreover, the methodology used to promote broadband depolarized high-efficiency responses via multilayer freeform metagratings can be applied not only to Littrow diffraction but also to other high-efficiency metasurfaces [48], such as anomalous

refraction and metalenses. Finally, in regard to the typical application of spectral laser beam combining, it ought to give some discussion on the requirements on laser beams in practice. For example, although there is no need for laser coherence in spectral combining, a narrow emission bandwidth and highly collimated beam profile of laser beams are typically required to achieve high output power and fine beam quality for the combining laser.

5. CONCLUSION

In conclusion, for the first time, we demonstrate a new essential functionality of broadband depolarized perfect Littrow diffraction via elegantly designed multilayer freeform metagratings. A typical example toward spectral laser beam combining application is designed to realize >99% unpolarized broadband efficiencies in a significant 60 nm bandwidth, which is much more superior to traditional diffractive approaches. The nontrivial performance results from the extremely flexible capability in tailoring the band structures and the field profiles of Bragg modes in metagratings to build a broadband constant π-phase difference for two polarization states simultaneously. Since the current EBL equipment has already been available for wafer-level fabrication, together with the efficient reproduction technique such as nanoimprint lithography, our work paves the way toward the practical application of Littrow gratings in, e.g., lasers, spectroscopy, and communications.

6. MATERIALS AND METHODS

Numerical simulation and optimization. An open source rigorous coupled-wave analysis (RCWA) solver, "RETICOLO" [49], was used to perform the full-wave simulation including the calculation of diffraction efficiency, interfacial phase, and the modal field profiles of Bragg modes. The topology optimization algorithm that we used is an open-source program supplied by Stanford University [50], which is performed iteratively and typically converges within 300 iterations. In the optimization process, an additional optimization procedure using a genetic algorithm was applied after each 10 iteration intervals, to optimize the height of metagratings and spacer thickness. The root mean square of the unpolarized broadband efficiency errors

$\mathrm{MF} = \left\{ \frac{1}{N} \sum_{j=1}^{N} \left(100\% - \frac{\eta_{\mathrm{TE}}(\lambda_j) + \eta_{\mathrm{TM}}(\lambda_j)}{2} \right)^2 \right\}^{1/2}$ at 1030–1090 nm is used as the merit function during optimization, where η refers to diffraction efficiency, and N is the number of wavelength points. More details about the implementation of topology optimization can be found in Ref. [41].

Sample fabrication. The HfO_2/SiO_2 multilayer mirror was first deposited on fused silica substrates using an electron beam evaporation plant OTFC1300 from Optorun. During deposition, an RF-type ion source was used to densify the deposited layers with a working condition of 250 V and 500 mA. The deposition temperature was set to 200°C, and the chamber was pumped down to a base pressure of 2.3×10^{-4} Pa. The deposition rates of HfO_2 and SiO_2 were 1.0 Å/s and 8.0 Å/s, respectively. Then, a layer of the positive electron beam resist (PMMA AR-672.08) with thickness of about 750 nm was spin-coated on the multilayer coatings, followed by baking for 10 min at 180°C. 10 nm of chromium was then coated on the sample surface by evaporation to avoid charging effects during EBL exposure. Next, the inverse patterns of the target metagratings were defined on the resist by EBL using a Raith EBPG 5200 system with 100 kV accelerator

voltage and 3 nA beam current. After exposure, the chromium was removed by a chromium remover, and the resist was developed in MIBK:IPA = 1:3 for 1 min. Next, the exposed resist patterns were filled by directly depositing HfO_2 using ALD at a low temperature (105°C) to avoid the glass transition of the resist. During the ALD process, a standard two-pulse system of water and tetrakis (dimethyl-lamino) hafnium (TDMAH) precursor was used with a 0.1 s water pulse and a 0.4 s TDMAH pulse. The ALD deposition rate was about 0.12 nm/cycle. Note that ALD finally leaves a redundant HfO_2 layer covering the resist surface, which should be removed to expose the beneath patterns. Therefore, we used inductively coupled reactive ion etching to remove the HfO_2 redundant layer with a mixture of CHF_3 and Ar gas (20 and 80 sccm, respectively) at a pressure of 15 mTorr. The inductively coupled plasma power was set to 800 W. The etching rate was about 0.6 nm/s. After this, the resist and the HfO_2 pattern below were exposed, and we used oxygen plasma to remove the remaining resist. The procedures of the microstructure preparation are also shown in Supplement 1 Note 6.

Sample characterization. The macro-region (R1) angle-resolved spectrum system (Ideaoptics, China) was used to characterize the broadband efficiency of the sample. The measurement realizes angle resolution by mechanically rotating the receiver. In the test, the intensity of incident light was detected via a high-reflection mirror. Then, the intensities of the −1st and zeroth order light were detected for all wavelengths to obtain the broadband efficiencies. The measurements were carried in a darkroom to improve the signal-to-noise ratio. Details of the efficiency measurement are given in Supplement 1 Note 7.

Disclosures. The authors declare no conflicts of interest.

Data availability. All data needed to evaluate the conclusions in the paper are present in the main text and the supplemental document. . The datasets generated and analyzed during this study are available from the corresponding author upon reasonable request.

Supplemental document. See Supplement 1 for supporting content.

REFERENCES

1. H. Lotem, "Littrow-mounted diffraction grating cavity," Appl. Opt. **33**, 930–934 (1994).
2. B. H. Kleemann, "Perfect blazing with echelle gratings in TE and TM polarization," Opt. Lett. **37**, 1002–1004 (2012).
3. N. Lyndin, M. Flury, S. Tonchev, R. Fechner, and O. Parriaux, "Design and fabrication of an all-dielectric grating with top-hat high diffraction efficiency over a broad spectral range," J. Eur. Opt. Soc. **2**, 5 (2007).
4. J. P. Wang, Y. X. Jin, J. D. Shao, and Z. X. Fan, "Optimization design of an ultrabroadband, high-efficiency, all-dielectric grating," Opt. Lett. **35**, 187–189 (2010).
5. Z. Varallyay and P. Dombi, "Design of high-efficiency ultrabroadband dielectric gratings," Appl. Opt. **53**, 5769–5774 (2014).

6. Y. J. Pang, Y. Zhang, H. Yang, Z. Liu, Z. Huang, and G. Jin, "Compact high-resolution spectrometer using two plane gratings with triple dispersion," Opt. Express **26**, 6382–6391 (2018).

7. B. Moslehi, P. Harvey, J. Ng, and T. Jannson, "Fiber-optic wavelength-division multiplexing and demultiplexing using volume holographic gratings," Opt. Lett. **14**, 1088–1090 (1989).

8. W. Jia, C. H. Zhou, J. J. Feng, and E. W. Dai, "Miniature pulse compressor of deep-etched gratings," Appl. Opt. **47**, 6058–6063 (2008).

9. K. R. Wei and L. F. Li, "Spectral beam combining gratings: high diffraction efficiency at a large deviation angle achieved around conical Littrow mounting," Opt. Lett. **46**, 4626–4629 (2021).

10. R. Ahmed, A. K. Yetisen, S. H. Yun, and H. Butt, "Color-selective holographic retroreflector array for sensing applications," Light Sci. Appl. **6**, e16214 (2017).

11. M. Britzger, A. Khalaidovski, B. Hemb, E. B. Kley, F. Brückner, R. H. Rinkleff, K. Danzmann, and R. Schnabel, "External-cavity diode laser in second-order Littrow configuration," Opt. Lett. **37**, 3117–3119 (2012).

12. A. V. Kildishev, A. Boltasseva, and V. M. Shalaev, "Planar photonics with metasurfaces," Science **339**, 1232009 (2013).

13. D. Lin, P. Fan, E. Hasman, and M. L. Brongersma, "Dielectric gradient metasurface optical elements," Science **345**, 298–302 (2014).

14. N. Yu and F. Capasso, "Flat optics with designer metasurfaces," Nat. Mater. **13**, 139–150 (2014).

15. S. Wang, P. C. Wu, V. C. Su, Y. C. Lai, M. K. Chen, H. Y. Kuo, B. H. Chen, Y. H. Chen, T. T. Huang, J. H. Wang, R. M. Lin, C. H. Kuan, T. Li, Z. Wang, S. Zhu, and D. P. Tsai, "A broadband achromatic metalens in the visible," Nat. Nanotechnol. **13**, 227–232 (2018).

16. S. Shrestha, A. C. Overvig, M. Lu, A. Stein, and N. Yu, "Broadband achromatic dielectric metalenses," Light Sci. Appl. **7**, 85 (2018).

17. Z. B. Fan, H. Y. Qiu, H. L. Zhang, X. N. Pang, L. D. Zhou, L. Liu, H. Ren, Q. H. Wang, and J. W. Dong, "A broadband achromatic metalens array for integral imaging in the visible," Light Sci. Appl. **8**, 67 (2019).

18. G. Zheng, H. Mühlenbernd, M. Kenney, G. Li, T. Zentgraf, and S. Zhang, "Metasurface holograms reaching 80% efficiency," Nat. Nanotechnol. **10**, 308–312 (2015).

19. L. Wang, S. Kruk, H. Tang, T. Li, I. Kravchenko, D. N. Neshev, and Y. S. Kivshar, "Grayscale transparent metasurface holograms," Optica **3**, 1504–1505 (2016).

20. Y. Hu, X. Luo, Y. Chen, Q. Liu, X. Li, Y. Wang, N. Liu, and H. Duan, "3D-Integrated metasurfaces for full-colour holography," Light Sci. Appl. **8**, 86 (2019).

21. H. Ren, G. Briere, X. Fang, P. Ni, R. Sawant, S. Héron, S. Chenot, S. Vézian, B. Damilano, V. Brändli, S. A. Maier, and P. Genevet, "Metasurface orbital angular momentum holography," Nat. Commun. **10**, 2986 (2019).

22. G. Y. Lee, J. Y. Hong, S. Hwang, S. Moon, H. Kang, S. Jeon, H. Kim, J. H. Jeong, and B. Lee, "Metasurface eyepiece for augmented reality," Nat. Commun. **9**, 1 (2018).

23. P. Huo, M. Song, W. Zhu, C. Zhang, L. Chen, H. J. Lezec, Y. Lu, A. Agrawal, and T. Xu, "Photorealistic full-color nanopainting enabled by a low-loss metasurface," Optica **7**, 1171–1172 (2020).

24. W. Yang, S. Xiao, Q. Song, Y. Liu, Y. Wu, S. Wang, J. Yu, J. Han, and D. P. Tsai, "All-dielectric metasurface for high-performance structural color," Nature Commun. **11**, 1 (2020).

25. L. Zhu, X. Liu, B. Sain, M. Wang, C. Schlickriede, Y. Tang, J. Deng, K. Li, J. Yang, M. Holynski, S. Zhang, T. Zentgraf, K. Bongs, Y. H. Lien, and G. Li, "A dielectric metasurface optical chip for the generation of cold atoms," Sci. Adv. **6**, eabb6667 (2020).

26. S. Divitt, W. Zhu, C. Zhang, H. J. Lezec, and A. Agrawal, "Ultrafast optical pulse shaping using dielectric metasurfaces," Science **364**, 890–894 (2019).

27. S. Sun, K. Y. Yang, C. M. Wang, T. K. Juan, W. T. Chen, C. Y. Liao, Q. He, S. Xiao, W. T. Kung, G. Y. Guo, L. Zhou, and D. P. Tsai, "High-efficiency broadband anomalous reflection by gradient meta-surfaces," Nano Lett. **12**, 6223–6229 (2012).

28. M. Khorasaninejad and K. B. Crozier, "Silicon nanofin grating as a miniature chirality-distinguishing beam-splitter," Nat. Commun. **5**, 5386 (2014).

29. F. Qin, L. Ding, L. Zhang, F. Monticone, C. C. Chum, J. Deng, S. Mei, Y. Li, J. Teng, M. Hong, S. Zhang, A. Alù, and C. W. Qiu, "Hybrid bilayer plasmonic metasurface efficiently manipulates visible light," Sci. Adv. **2**, e1501168 (2016).

30. N. Yu, P. Genevet, M. A. Kats, F. Aieta, J. P. Tetienne, F. Capasso, and Z. Gaburro, "Light propagation with phase discontinuities: generalized laws of reflection and refraction," Science **334**, 333–337 (2011).

31. A. Díaz-Rubio, V. S. Asadchy, A. Elsakka, and S. A. Tretyakov, "From the generalized reflection law to the realization of perfect anomalous reflectors," Sci. Adv. **3**, e1602714 (2017).

32. T. He, T. Liu, S. Xiao, Z. Wei, Z. Wang, L. Zhou, and X. Cheng, "Perfect anomalous reflectors at optical frequencies," Sci. Adv. **8**, eabk3381 (2022).

33. Z. L. Deng, J. Deng, X. Zhuang, S. Wang, T. Shi, G. P. Wang, Y. Wang, J. Xu, Y. Cao, X. Wang, X. Cheng, G. Li, and X. Li, "Facile metagrating holograms with broadband and extreme angle tolerance," Light Sci. Appl. **7**, 78 (2018).

34. N. M. Estakhri and A. Alu, "Wave-front transformation with gradient metasurfaces," Phys. Rev. X **6**, 041008 (2016).

35. Y. Ra'di, D. L. Sounas, and A. Alù, "Metagratings: beyond the limits of graded metasurfaces for wave front control," Phys. Rev. Lett. **119**, 067404 (2017).

36. A. M. Wong and G. V. Eleftheriades, "Perfect anomalous reflection with a bipartite Huygens' metasurface," Phys. Rev. X **8**, 011036 (2018).

37. E. Khaidarov, H. Hao, R. Paniagua-Domínguez, Y. F. Yu, Y. H. Fu, V. Valuckas, S. L. K. Yap, Y. T. Toh, J. S. K. Ng, and A. I. Kuznetsov, "Asymmetric nanoantennas for ultrahigh angle broadband visible light bending," Nano Lett. **17**, 6267–6272 (2017).

38. Z. Fan, M. R. Shcherbakov, M. Allen, J. Allen, B. Wenner, and G. Shvets, "Perfect diffraction with multiresonant bianisotropic metagratings," ACS Photon. **5**, 4303–4311 (2018).

39. A. Patri, S. Kena-Cohen, and C. Caloz, "Large-angle, broadband, and multifunctional directive waveguide scatterer gratings," ACS Photon. **6**, 3298–3305 (2019).

40. T. Phan, D. Sell, E. W. Wang, S. Doshay, K. Edee, J. Yang, and J. A. Fan, "High-efficiency, large-area, topology-optimized metasurfaces," Light Sci. Appl. **8**, 48 (2019).

41. D. Sell, J. Yang, S. Doshay, R. Yang, and J. A. Fan, "Large-angle, multifunctional metagratings based on freeform multimode geometries," Nano Lett. **17**, 3752–3757 (2017).

42. J. Jiang, D. Sell, S. Hoyer, J. Hickey, J. Yang, and J. A. Fan, "Freeform diffractive metagrating design based on generative adversarial networks," ACS Nano **13**, 8872–8878 (2019).

43. Z. Shi, A. Y. Zhu, Z. Li, Y. W. Huang, W. T. Chen, C. W. Qiu, and F. Capasso, "Continuous angle-tunable birefringence with freeform metasurfaces for arbitrary polarization conversion," Sci. Adv. **6**, eaba3367 (2020).

44. P. Lalanne, J. P. Hugonin, and P. Chavel, "Optical properties of deep lamellar gratings: a coupled Bloch-mode insight," J. Lightwave Technol. **24**, 2442–2449 (2006).

45. S. Tang, B. Zhu, M. Jia, Q. He, S. Sun, Y. Mei, and L. Zhou, "Effective-medium theory for one-dimensional gratings," Phys. Rev. B **91**, 174201 (2015).

46. T. Clausnitzer, T. Kämpfe, E. B. Kley, A. Tünnermann, U. Peschel, A. V. Tishchenko, and O. Parriaux, "An intelligible explanation of highly-efficient diffraction in deep dielectric rectangular transmission gratings," Opt. Express **13**, 10448–10456 (2005).

47. I. Kim, S. So, J. Mun, K. H. Lee, J. H. Lee, T. Lee, and J. Rho, "Optical characterizations and thermal analyses of HfO_2/SiO_2 multilayered diffraction gratings for high-power continuous wave laser," J. Phys. Photon. **2**, 025004 (2020).

48. H. Jeong, Y. Yang, H. Cho, T. Badloe, I. Kim, R. M. Ma, and J. Rho, "Emerging advanced metasurfaces: alternatives to conventional bulk optical devices," Microelectron. Eng. **220**, 111146 (2020).

49. J. P. Hugonin and P. Lalanne, *Reticolo Software for Grating Analysis* (Institut d'Optique, 2005).

50. J. Jiang, R. Lupoiu, E. W. Wang, D. Sell, J. P. Hugonin, P. Lalanne, and J. A. Fan, "MetaNet: a new paradigm for data sharing in photonics research," Opt. Express **28**, 13670–13681 (2020).